International Journal of Rock Mechanics & Mining Sciences 178 (2024) 105756

Contents lists available at ScienceDirect

International Journal of Rock Mechanics and Mining Sciences

journal homepage: www.elsevier.com/locate/ijrmms

Application of three-component acoustic emission sensor in rock mechanics experiments

Shan Wu [a], Ke Gao [b,*], Yunyi Qian [c,**], Hongkui Ge [d], Xiaoqiong Wang [d], Tiantai Li [e]

[a] School of Resource and Environmental Engineering, Hefei University of Technology, Hefei 230009, Anhui, China
[b] Department of Earth and Space Sciences, Southern University of Science and Technology, Shenzhen, 518055, Guangdong, China
[c] School of Resources and Safety Engineering, Chongqing University, Chongqing, 400044, China
[d] State Key Laboratory of Petroleum Resources and Prospecting, China University of Petroleum (Beijing), Beijing, 102249, China
[e] Department of Petroleum Engineering, Xi'an Shiyou University, Xi'an, 710065, Shanxi, China

ARTICLE INFO

Keywords:
Acoustic emission
Three-component sensor
Polarization analysis
Rock fracture
Rock failure

ABSTRACT

In laboratory rock mechanics experiments, it is common practice to employ single-component acoustic emission (AE) sensors to monitor the rock fracturing process, where the fracture location and fracturing mechanism can be inverted from the single-component AE waveforms. However, since such applications are often based on simplified isotropic hypotheses, accurately capturing the influence of strong anisotropy in rock on particle vibrations at rock surfaces using single-component AE sensors remains challenging. This limitation biases the actual particle vibration amplitude and direction, potentially leading to erroneous estimations in AE waveform inversion mof rock fracturing. Here, we combined three piezoelectric discs to create a three-component AE sensor, allowing us to capture particle vibration along three sensing directions on rock surfaces. Through two calibration experiments and polarization analysis of the three-component waveforms, we verify the new sensor's capability to reliably capture the vibration features of hypocenters that are not easily obtainable using a single-component sensor. We apply this new sensor in uniaxial compression tests on shale, a material known for its strong anisotropy. The results indicate that the AE behaviors monitored by the three-component sensor are consistent with those obtained from the widely used single-component sensor. Moreover, the polarization analysis of the three-component waveforms reveals the presence of coupled hypocenters associated with multiple fractures. This is the first time a three-component AE sensor is used in laboratory rock mechanics experiments, which offers a more comprehensive understanding of the dynamic evolution of fractures in rock formations.

1. Introduction

The application of acoustic emission (AE) monitoring is commonplace in many aspects of rock mechanics, such as the evaluation of rock failure and the investigation of fracture propagation mechanisms in hydraulic fracturing.[1–4] In general, AE is the release of elastic energy induced by damages, fractures, and disturbance of local stresses inside rocks,[3,5–8] which is usually regarded as earthquakes in laboratory scale and high-frequency domain (kHz and MHz).[9–12] The study of the mechanism of AE can deepen the understanding of the rock failure process and assist the safe construction of rock engineering projects.

Nearly all the currently employed AE sensors can only collect AE signals from the direction perpendicular to the sensor's surface (i.e., the surface of piezoelectric ceramic), i.e., the so-called single-component AE sensor[40]. One important reason for the wide use of single-component AE sensors lies in their high sensitivity to the generation of signals, which obeys the original design purpose of AE monitoring for damage detection inside an object.[13] However, the single-component AE sensors restrict the application of AE monitoring in aspects that call for fracture location and focal mechanism inversion. Specifically, for fracture location, only the first arrival phase of the waveform, i.e., the *P*-wave, can be effectively identified using a single-component AE senor,[14,15] with other waveform phases difficult to differentiate. Additionally, a single-component sensor does not directly capture the polarity and amplitude of the waveform, both of which are essential for the inversion of the focal mechanism of AE hypocenters. Furthermore, in these

* Corresponding author.
** Corresponding author.
E-mail addresses: gaok@sustech.edu.cn (K. Gao), qianyy@cqu.edu.cn (Y. Qian).

https://doi.org/10.1016/j.ijrmms.2024.105756
Received 7 January 2024; Received in revised form 21 April 2024; Accepted 4 May 2024

AE-related practices, the rock material is always assumed to be isotropic, so the complete amplitude of waveform can be calculated based on the assumption that the direction from the hypocenter to the AE sensor coincides with the particle vibration direction. Then, the simplified moment tensor method proposed by Ohtsu[16] can be used to inverse the focal mechanism of an AE event. With such a common "isotropic" assumption, the calculated waveform amplitude based on the single-component waveforms may have non-neglectable errors, especially for highly isotropic rocks. Albeit with many problems, AE sensors currently applied in rock mechanics experiments are all single-component. This may also be due to their simple structure and ease of fabrication.

Theoretically, an AE sensor having three orthogonal components may eliminate the deficiencies in single-component sensors. First, the three-orthogonal vibrations from a sensor can synthesize the accurate waveforms by summating the three vectors of vibrations without hypothesis, although this may sacrifice the sensor sensitivity slightly. Furthermore, the *P*- and *S*-wave can be distinguished by the polarization analysis of three-component waveforms. With the information in both the *P*- and *S*-wave, a more precise analysis of the location and focal mechanism of AE hypocenters can be achieved.[17–20] Moreover, the accurate waveforms provided by a three-component sensor can promote the exploration of the absolute physical meaning of AE waveforms, which is important in inversion problems. Generally, the single-component AE waveform has unclear physical meaning due to the uncertain connection between the vibration sensed by a piezoelectric ceramic plate and the displacement, velocity, and acceleration of materials.[21,22] Additionally, calibrating a single-component sensor is usually difficult,[11,23] and thus the amplitude of AE waveforms recorded by single-component sensors has always been expressed by relative magnitudes. Although most monitoring strategies select single-component sensors at multiple positions to compensate for those defects, it is still necessary to employ new three-component sensors in laboratory AE monitoring, just like that in the seismology field where three-component instruments are commonly used.[22] To the best of our knowledge, only single-component sensors are currently widely provided commercially. In contrast, three-component sensors are hardly seen in AE monitoring, probably due to the obstacles to coordinating and synchronizing vibrations from three directions at one detection point by piezoelectric discs.

In this paper, we fabricate a three-component sensor consisting of three piezoelectric discs. To test the performance of the three-component sensor, we conduct two calibration experiments to acquire the three-component waveforms. We apply the polarization analysis on the waveforms to obtain the hypocenters' characteristics, and then discuss the applicability of the three-component sensor in a uniaxial compression experiment. The paper is organized as follows. In Section 2, we show the structure of the three-component sensor and briefly introduce the polarization analysis of three-component waveforms. Section 3 presents the characteristics of three-component waveforms obtained from ultrasonic, dropping ball testing, and uniaxial compression experiments. Finally, we discuss the preliminary and further application of three-component AE sensors in rock fracturing processes and conclude at the end.

2. Device and methods

2.1. Three-component AE sensor

The structure of the three-component AE sensor is shown in Fig. 1a, which consists of three piezoelectric ceramic plates glued and stacked on each other, along with the damping unit. Plate *P* receives vibrations perpendicular to the sensor surface, and plates *S*1 and *S*2 receive vibrations tangential to the sensor surface in two orthogonal directions. The three piezoelectric ceramic plates are vibrated when an AE waveform arrives at the sensor. The waveform can be decomposed into three directions, as shown in Fig. 1b. In the coordinate system aligned with the three sensing directions of the sensor, the incident direction of the waveform can be characterized by two angles, i.e., the dip angle α and the azimuth angle φ (Fig. 1b), which can be obtained by the polarization analysis introduced next.

2.2. Polarization analysis

Waveforms in the three directions represent the corresponding particle vibration traces. The study of particle vibration traces is called polarization analysis, in which the change of particle vibration trace indicates the phase change in the waveform. Since the 1960s, polarization analysis of seismic waveforms has gained increasing attention[24] and is an effective method for separating *P*- and *S*-wave. The polarization of waveform is the time-space characteristic of particle vibration. Different waveform phases indicate different polarization directions.[25] The longitudinal wave (*P*-wave) is linearly polarized if the *P*-wave is not coherent with other waves. The direction of particle vibration of *P*-wave is consistent with its propagation direction. The transverse wave (*S*-wave) is also linearly polarized, but its direction of particle vibration is perpendicular to its propagation direction. Additionally, there are also surface waves elliptically polarized in the vertical plane.[7,26]

The linearity and direction of polarization can be computed based on a covariance matrix,[27]

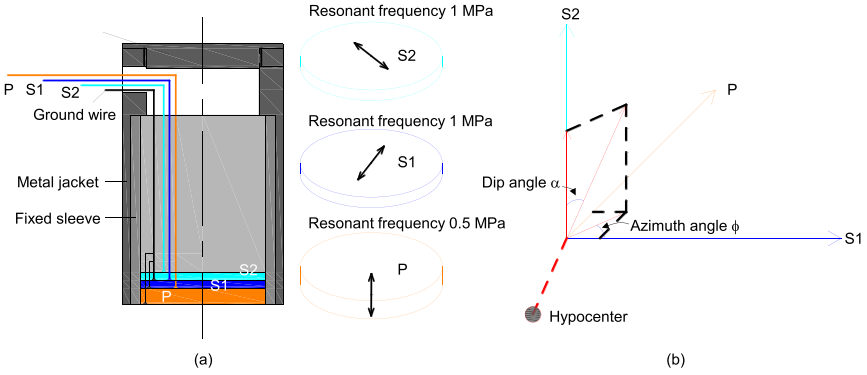

Fig. 1. (a) The structure of the three-component AE sensor. (b) Decomposition of particle vibration in the coordinate system coincided with the three sensing directions of the sensor (the red line represents the direction of initial particle vibration). (For interpretation of the references to colour in this figure legend, the reader is referred to the Web version of this article.)

$$\mathbf{V}=\begin{bmatrix} \mathrm{var}(x) & \mathrm{cov}(x,y) & \mathrm{cov}(x,z) \\ \mathrm{cov}(x,y) & \mathrm{var}(y) & \mathrm{cov}(y,z) \\ \mathrm{cov}(x,z) & \mathrm{cov}(y,z) & \mathrm{var}(z) \end{bmatrix}, \tag{1}$$

where $\mathrm{cov}(x,y)$, $\mathrm{cov}(y,z)$ and $\mathrm{cov}(x,z)$ are the covariances among the waveform data in the x, y, and z directions; the $\mathrm{var}(x)$, $\mathrm{var}(y)$ and $\mathrm{var}(z)$ denote the corresponding variances. The covariance can be calculated by

$$\mathrm{cov}(x,y)=\frac{1}{N}\sum_{i=1}^{N}(x_i-\mu_x)\left(y_i-\mu_y\right), \tag{2}$$

where μ_x, μ_y and μ_z are the averages of waveform data in the x, y, and z-direction, respectively. The three eigenvalues and eigenvectors of the covariance matrix $\mathbf{V}$ are λ_i and $\mathbf{v}_i$, where $i=1,2,3$ and we assume $\lambda_1 \geq \lambda_2 \geq \lambda_3$. The eigenvectors represent the main polarization direction of the recorded waveforms (Kanasewich, 1981; Lin et al., 2012), and the eigenvalues reflect the linearity of polarization. The waveform with pure linear polarization, such as the *P*-wave, *S*-wave, and Love surface wave, has only one non-zero eigenvalue (i.e., $\lambda_1 \neq 0, \lambda_2 = 0, \lambda_3 = 0$). The waveform with pure elliptic polarization, such as the Rayleigh wave, has two non-zero eigenvalues (i.e., $\lambda_1 = \lambda_2 \neq 0, \lambda_3 = 0$). Generally, the three eigenvalues of waveform data are non-zero and do not equal each other.

The linearity of polarization is quantified by a linear parameter called rectilinear (RL), which also describes the shape of particle vibration trace. There are several ways to calculate rectilinear.[25,28,29] In the present paper, we use the method presented in Jurkevics[25] to calculate RL, i.e.,

$$\mathrm{RL}=\left(1-\frac{\lambda_2+\lambda_3}{2\lambda_1}\right)\times 100\%. \tag{3}$$

RL = 1 and RL = 0 respectively correspond to pure linear and pure elliptic polarization. The dip angle α and the azimuth angle φ of the waveform can be calculated by the direction of polarization, i.e.,

$$\alpha=\arctan\frac{\sqrt{{v_{1x}}^2+{v_{1y}}^2}}{v_{1z}} \tag{4}$$

and

$$\varphi=\arctan\frac{v_{1y}}{v_{1x}}, \tag{5}$$

where v_{1x}, v_{1y} and v_{1z} are the components of $\mathbf{v}_1$ in the three sensing directions x, y, and z, respectively. Here, $\mathbf{v}_1$ is the principal direction of particle vibration corresponding to λ_1.

The polarization analysis can identify the different phases of the waveform even in complex wavefields where multiple phases of waveform overlap each other. It should be noted that the length of the time window used for waveform calculation needs to be determined according to the sampling rate and the dominant frequency of the waveform. If the time window is too small, the polarization parameters are over-sensitive, and the results may exhibit abrupt changes. If the time window is too large, the polarization may be dull, and the change of the waveform phase may not be identified accurately.

3. Experiments and results

In this section, we conduct two calibration tests, i.e., an ultrasonic test and a dropping ball test, to facilitate the evaluation of the new sensor's monitoring capability. We utilize polarization analysis of the three-component waveforms to calibrate their relationship with the ultrasonic and dropping ball seismic sources. Then, we apply the three-component sensor in uniaxial compression experiments on shale and discuss its effectiveness in the context of rock mechanics testing.

3.1. Ultrasonic testing

Ultrasonic testing involves the active generation of ultrasonic vibrations, which are then received by the acoustic emission sensor. The ultrasonic seismic source's short duration can be considered a pulse source, making it convenient for calibrating the sensor's response. We use a commercial piezoelectric sensor V153 with a 1 MHz resonant frequency (Olympus Ltd.) to generate a mechanical motion as the hypocenter on the left side of the cylindrical steel bar. The three-component sensor acts as the receiver on the right (Fig. 2). The mechanical motion of V153 is caused by a rectangular electric pulse generated by a pulse/receiver 5077 PR (Olympus Ltd.) and then initiates the elastic wave in the steel cylinder with a *P*-wave velocity of 6200 m/s and an *S*-wave velocity of 3300 m/s. The elastic waves from the transmit point can induce both normal (*P*-wave) and tangential (*S*-wave) motions. We employ an AE acquisition system to record the receiver's waveforms at a sampling rate of 10 MHz. Fig. 3a presents the waveforms received by the three-component AE sensor, from which we can see that the high amplitude in the waveform at ~30 μs represents the arrival of the *S*-wave (red line), and the low amplitude at the beginning segment of the waveform shows the arrival of the *P*-wave (blue line). We then draw the particle motion traces of the waveforms in Fig. 3b, where the blue and red lines represent the particle motion plotted with the *P*- and *S*-wave segments, respectively. It can be seen that the particle motion trace in the *P*-wave stage is parallel to the *P*-direction. When the *S*-wave is generated, the particle motion trace begins tilting to the direction parallel to the *S*-direction. These are consistent with the characteristics of the *P*- and *S*-wave particle traces generated by sensor V153.[30]

We apply the polarization analysis for the waveforms to obtain the rectilinear, dip angle, and azimuth angle (Fig. 4). The *P*- and *S*-wave have linear polarization, so the rectilinear is close to 1. However, there are fluctuations in rectilinear before the arrival of the *P*- and *S*-wave. This may be caused by the vibration inertia of the sensor or the noise from the electrical signal conversion. According to Fig. 4, the dip angle of the *P*-wave is close to 0 (blue line), and the dip angle of the *S*-wave is about 15° (red line). The azimuth angle of the *P*-wave is close to 10° (blue line), and the azimuth angle of the *S*-wave is about 100° (red line). Since the particle motion direction of the *S*-wave is the back-and-forth motion of particles in the plane, both −100° and 100° are the appropriate azimuth angle for the *S*-wave. After the first 35 μs, several jitters can be seen in the three curves behind the *S*-wave segment (Fig. 4). This is due to the coherent effect of ultrasonic waves inside the rock. Under the test condition presented here, theoretically, the dip angle of the *P*-wave should be close to 0, the dip angle of the *S*-wave should be between 0 and 90°, and the azimuth angle of the *P*-wave should differ from that of the *S*-wave by 90°. The polarization results above are within the reasonable range of the theoretical values. It can be concluded that the characteristics of the *P*- and *S*-wave from the particle vibration can be distinguished, although the waveform coherence brings some interference. This means utilizing the three-component AE sensor can effectively distinguish different wave phases through polarization analysis.

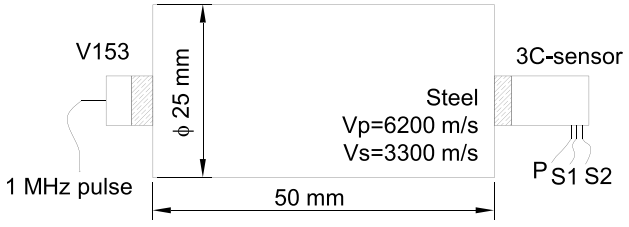

Fig. 2. Illustration of the ultrasonic testing.

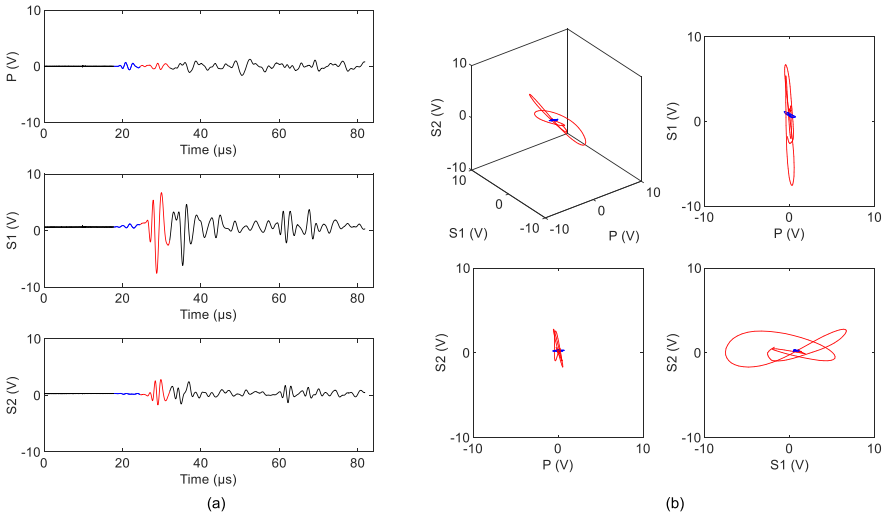

Fig. 3. (a) Three-component waveforms of the ultrasonic testing. (b) Particle motion trace of the ultrasonic testing. The black line represents the waveform, the blue section corresponds to the *P*-wave, and the red section corresponds to the *S*-wave. (For interpretation of the references to colour in this figure legend, the reader is referred to the Web version of this article.)

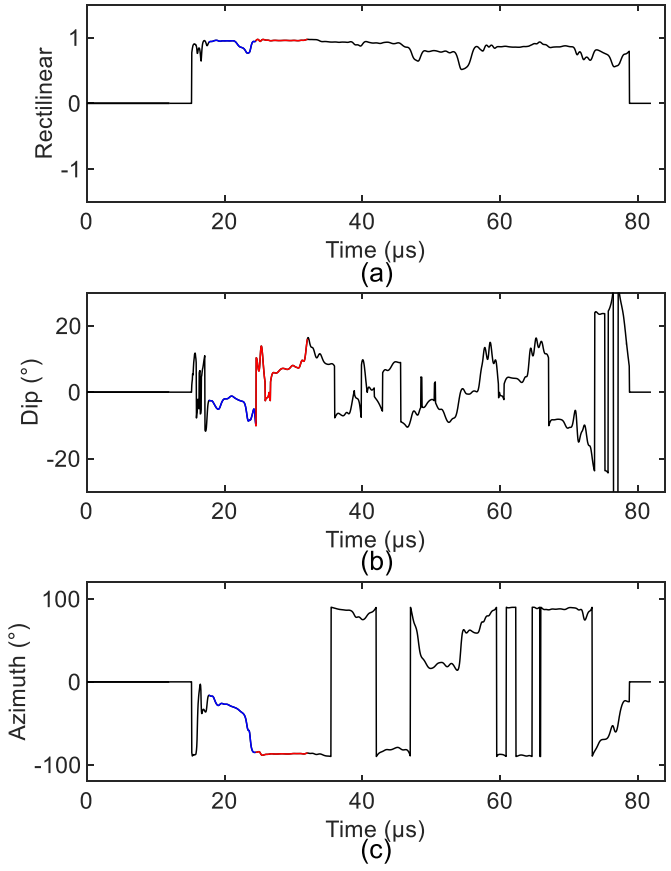

Fig. 4. (a) Rectilinear, (b) dip angle, and (c) azimuth angle of the ultrasonic testing. The black line represents the waveform, the blue section corresponds to the *P*-wave, and the red section corresponds to the *S*-wave. (For interpretation of the references to colour in this figure legend, the reader is referred to the Web version of this article.)

3.2. Ball drop testing

Ball drop testing is widely used to calibrate AE sensors.[21,31] Through the test, we can calculate the energy, velocity, and acceleration of the dropping ball by a loading function, including the height of the drop and the mass of the ball, which makes it convenient to calibrate the absolute physical sense of the sensor. Gu et al.[31] recapitulated the loading function of the ball drop as

$$f(t) = -F_{\max} \sin\left(\frac{\pi t}{t_c}\right)^{3/2}, 0 \le |t| \le t_c, \quad f(t) = 0, \text{otherwise} \tag{6}$$

where $F_{\max}$ is the maximum loading force during the contact process of the dropping ball and the contact sample, and t_c is the total time of the contact process. The $F_{\max}$ and t_c are modeled as

$$\begin{aligned} F_{\max} &= 1.917\rho_1{}^{3/5}(\delta_1+\delta_2)^{-2/5}R_1^2 v_0^{6/5} \\ \delta_q &= \frac{1-\mu_q^2}{\pi E_q}, q = 1,2 \\ t_c &= 1\Big/f_c = 4.53(4\rho_1\pi(\delta_1+\delta_2)/3)^{2/5}R_1 v_0^{-1/5} \\ v_0 &= \sqrt{2gh} \end{aligned} \tag{7}$$

where ρ_q, E_q, u_q are the density, Young's modulus, and Poisson's ratio of the material q, respectively ($q = 1$ refers to the steel ball, and $q = 2$ refers to the contact sample). Based on the loading function, we sketch in Fig. 5 the wavefield from a ball dropping that contains an obvious *P*-wave.

In this experiment, the AE system records a short waveform (sampling rate 10 MHz) followed by an overflow distortion due to the overflow signal caused by the large energy of the dropping ball. Only a short segment of the waveform, corresponding to *P*-wave vibration, can be used for the following analysis (Fig. 6a). We conduct the polarization analysis for this waveform segment, and the results are shown in Fig. 6b. The analysis gives a rectilinear parameter of 1, and the dip angle and azimuth angle remain stable, which are consistent with the characteristics of the hypocenter of the dropping ball. This further demonstrates that the three-component AE sensor can reliably reflect the particle vibrations.

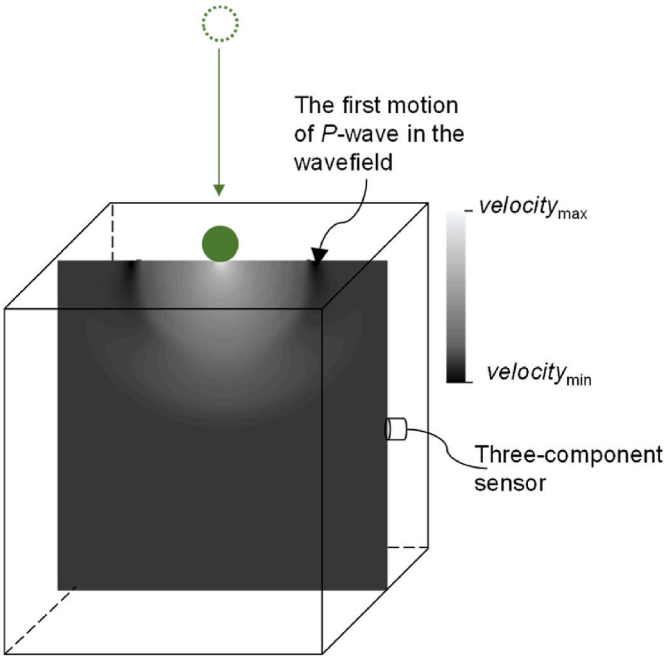

Fig. 5. The sketch of the wavefield in a ball drop testing.

3.3. Uniaxial compression testing

Natural fractures in shale affect its fracturing process, which is an essential mechanical problem in oil and gas production.[32] Uniaxial compression experiments together with AE monitoring are commonly used to investigate the characteristics of rock failure in shale. Here, we apply the three-component AE sensor to monitor a uniaxial compression experiment on a shale specimen to check whether the AE waveforms could reflect the complicated rock failure mechanisms. The shale samples were obtained from the Jilin shale oil-producing region in China and prepared in a cylindrical shape with a diameter of 25 mm and a height of 50 mm. The testing was conducted using the Geotechnical Consulting and Testing Systems (GCTS) mode RTR 2000, as shown in Fig. 7. To compare the results with the traditional single-component sensor, a commercial sensor – Nano30 – from *Physical Acoustics Company* is also used in the experiment (Fig. 7). We choose the continuous acquisition method to obtain the AE waveforms, and a 10 MHz sampling rate is employed. The velocities of *P*- and *S*-wave in shale used in the experiment are 4101 m/s and 2710 m/s, respectively.

Fig. 8a shows the stress-strain curve of the uniaxial compression test together with the AE rates from both the single-component and the three-component sensors. It is shown that fewer AE events are acquired by the three-component sensor (red line) compared with the single-component sensor (gray line). Nevertheless, the trend of AE rate changes for the two sensors is consistent. We then compare the distribution of AE event amplitude by the log N_{AE} versus M_{AE} curve in Fig. 8b, where M_{AE} is the AE amplitude in unit dB, and N_{AE} is the number of AE with an amplitude larger than M_{AE}. These curves demonstrate the characteristics of the failure process of the shale specimen and can reflect the performance of the sensors. Fig. 8b indicates that the slopes of the two curves are almost parallel in the amplitude range smaller than 2.5, demonstrating that the two sensors have a similar response to the amplitude distribution in the rock failure process. However, the single-component sensor is more sensitive to AE with large amplitudes (higher than 2.5) than the three-component sensor, which is manifested by the fact that the single-component sensor collects a higher proportion of events with an amplitude larger than 2.5. This is probably because AE events with higher amplitudes are usually of lower frequency, and the single-component sensor is more sensitive to lower-frequency AE events than the three-component sensor. Nevertheless, the three-component sensor presents a similar AE rate and amplitude distribution to the single-component sensor in the uniaxial compression test.

We further investigate the three-component waveforms for analyzing the fracture hypocenters during the uniaxial compression test. Typical waveforms from the compression, elastic, and plastic stages of the uniaxial compression process are selected for the analysis. The compression stage, represented by the initial nonlinear portion of the stress-strain curve, indicates crack closure. This is followed by the elastic stage, characterized by linear stress-strain behavior, and then the plastic stage, which extends from the end of the elastic stage to the peak stress. The waveforms and results of polarization analysis for the three stages are respectively presented on the left and right columns of Fig. 9, Fig. 10,

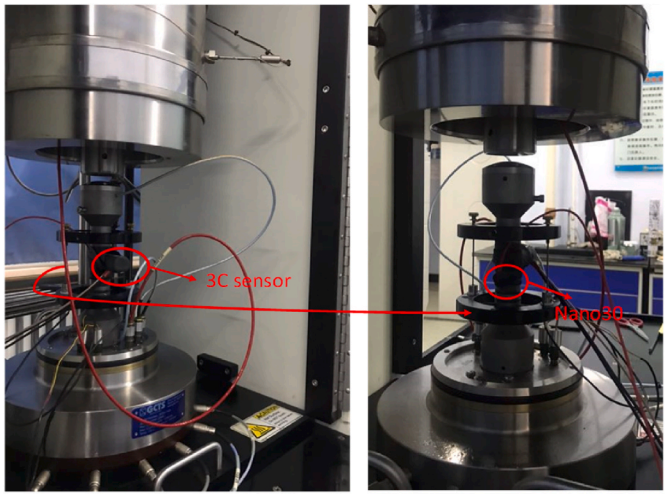

Fig. 7. Uniaxial compression testing with Nano30 and the three-component AE sensor.

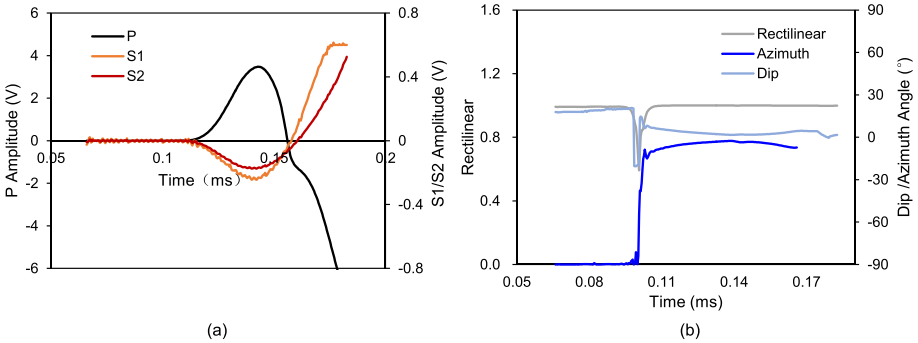

Fig. 6. (a) Waveforms and (b) polarization analysis of ball dropping testing.

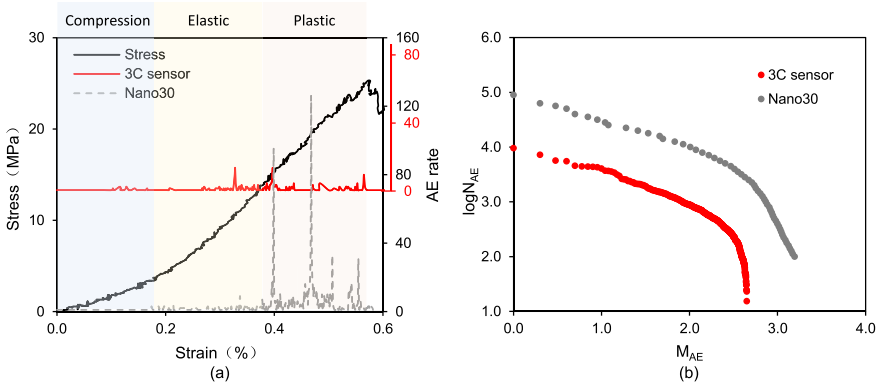

Fig. 8. Results of the uniaxial compression testing. (a) The strain-stress curve and AE rates with respect to axial strain. (b) The AE amplitude distribution curves for the two sensors. Here, "3C" denotes "three-component".

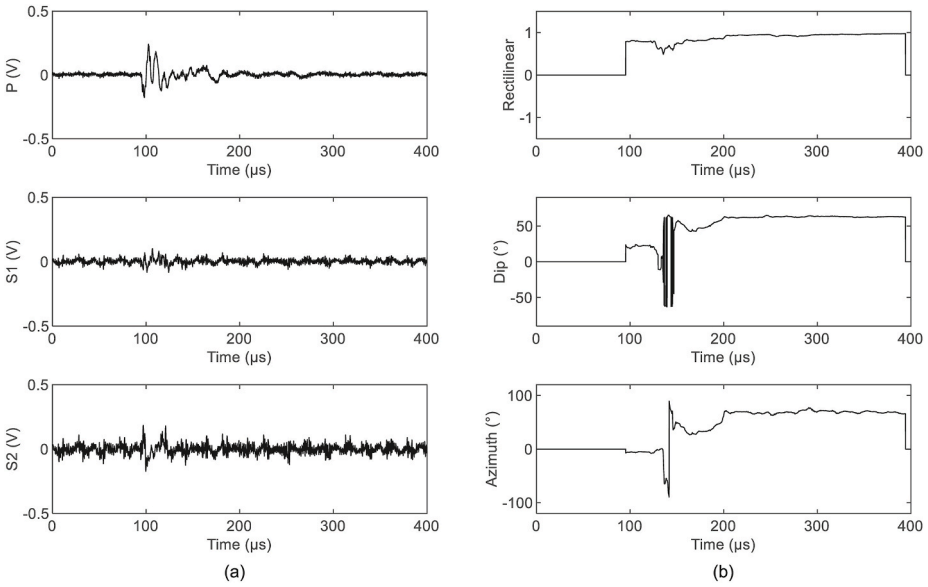

Fig. 9. Typical AE events in the compression stage of the uniaxial compression testing. (a) Waveforms from the three-component sensor. (b) Polarization analysis of the waveforms.

and Fig. 11. The mechanism of fractures in the compression stage is straightforward (Fig. 9), which is usually caused by the closure of fractures. Consequently, fracture closure results in simple source mechanisms, which can be reflected in the waveform. We observe in the waveform that the rectilinear value exhibits fluctuations primarily at the beginning, with the dip angle and azimuth angle displaying a similar changing trend. The mechanism of the fractures in the elastic stage becomes more complex (Fig. 10), so the rectilinear, dip angle and azimuth angle oscillate continuously. It can be seen from the curve of the dip angle that there are two small changes with short intervals around 100 μs, and two large changes at 200 μs and 350 μs. These changes are not induced by the different waveform phases from the same hypocenter but by the different hypocenters from various times or diverse positions. This indicates that the AE waveforms contain mixed mechanical hypocenters. The AE waveform in the plastic stage is even more multifarious (Fig. 11). The dramatic changes in the polarization curves reflect the occurrence of multiple fractures, as they are closely aligned in both time and space, resulting in complex seismic sources.

4. Discussion

From the three experiments presented above, we preliminarily test the applicability of the three-component sensor in the process of AE monitoring in rock experiments. Although the current experimental results show that the three-component waveforms can distinguish the polarization parameters for different phases of the waveforms, there is no quantitative criterion to separate them. In the future, experiments are still needed to calibrate the three-component sensor with the ultimate goal of reaching a theoretical model for the quantitative interpretation of the waveforms in the rock failure process. Future research could develop specific quantitative metrics based on characteristics such as rectilinear, dip angle, azimuth angle, amplitude ratio and frequency content. Statistical analysis could help establish threshold values that effectively differentiate waveform phases under various conditions. Additionally, applying machine learning techniques could greatly improve automatic classification and distinction of waveform phases. Techniques like support vector machines (SVM) or neural networks could be employed, trained on datasets with pre-identified waveform phases from extensive pre-testing.

Moreover, the uniaxial compression tests using single-component and the three-component sensor, as shown in Fig. 8, reveal lower sensitivity in the three-component sensor. The single-component sensor recorded 1556 AE hits, compared to only 448 AE hits by the three-component sensor. Despite having similar resonant frequencies—750

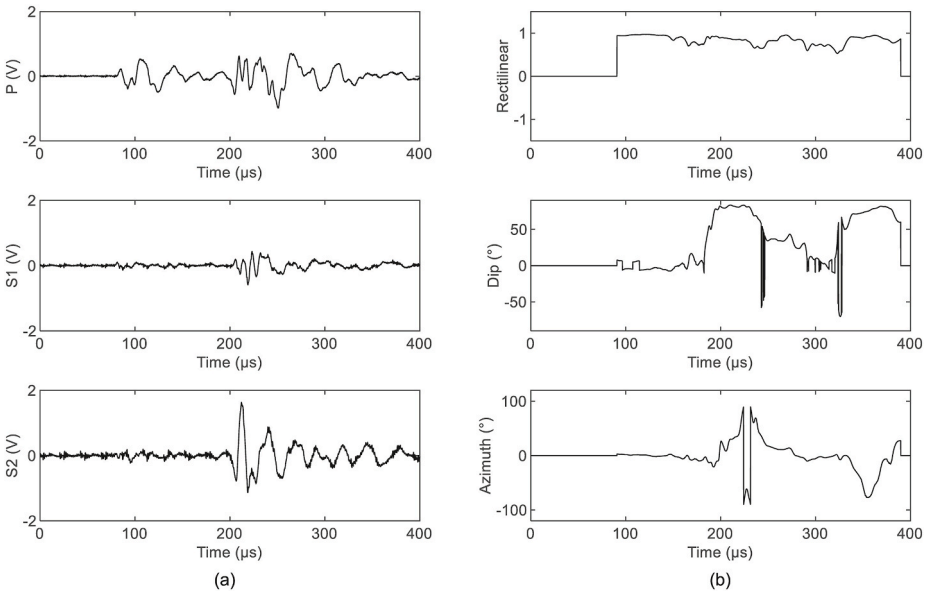

Fig. 10. Typical AE events in the elastic stage of the uniaxial compression testing. (a) Waveforms from the three-component sensor. (b) Polarization analysis of the waveforms.

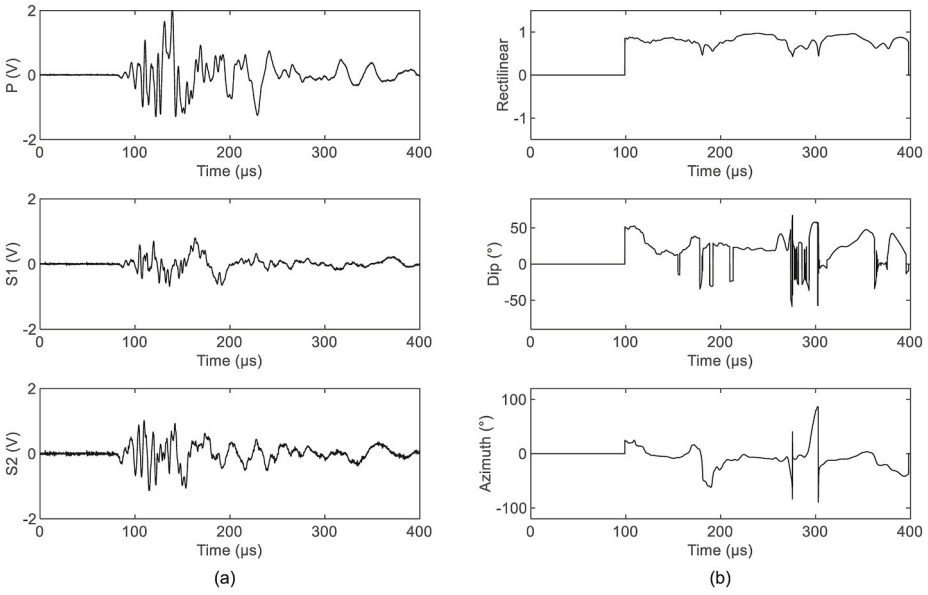

Fig. 11. Typical AE events in the plastic stage of the uniaxial compression testing. (a) Waveforms from the three-component sensor. (b) Polarization analysis of the waveforms.

kHz for the single-component sensor and 500 kHz for *P*-waves, 1 MHz for *S*-waves in the three-component sensor—the difference in reception is significant. This suggests a considerable loss in signal sensitivity for the three-component sensor. A probable cause is that three piezoelectric ceramic plates need to be vibrated by the source, which is less efficient for low-energy sources. A potential solution is to integrate a signal amplification unit upfront to enhance energy delivery and improve the signal-to-noise ratio. This method has been successful in Glaser-type sensors, producing low-energy, high signal-to-noise ratio signals.[33,34] Enhancing multi-component probes with pre-energy amplification could improve the utility of AE monitoring in analyzing micro-fractures.

The polarization analysis of the three-component waveforms can distinguish the special waveform phases. This could advance a novel AE location method that utilizes both hypocenter direction and the time arrival delay between *P*- and *S*-waves through a single three-component sensor, assuming isotropic rock properties. The ratio of the amplitude of the three-component waveforms can determine the direction of the hypocenter, as shown in Fig. 12. The difference in the arrival time of *P*- and *S*-waves can determine the distance between sensors and the hypocenter as follows,

$$t_P^{arrival} = t_0 + \Delta/V_P, t_S^{arrival} = t_0 + \Delta/V_S, \tag{8}$$

where t_0 is the initial time of the hypocenter, Δ is the distance between the hypocenter and the sensor and is given by

$$\Delta = \left(t_P^{arrival} - t_S^{arrival}\right)\frac{V_P V_S}{V_P - V_S}. \tag{9}$$

In the uniaxial compression experiment, a total of 448 distinct AE events were recorded. Because the size of the specimen used in this test is small, the *P*- and *S*-waves can be clearly distinguished in the

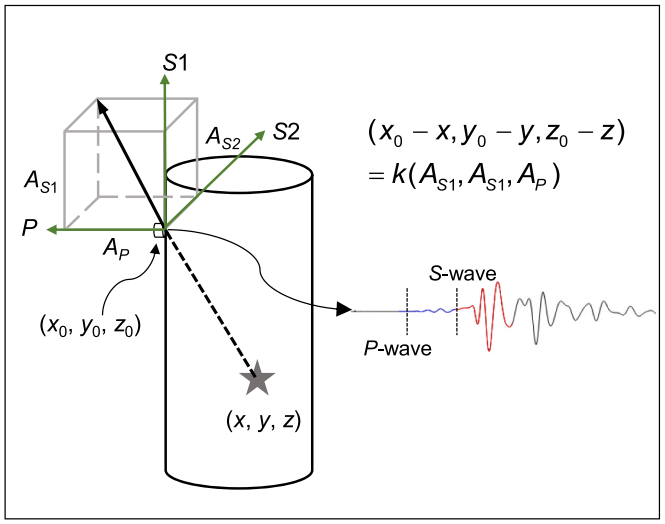

Fig. 12. The *P*-wave first motions in the three-component waveforms. The star represents the hypocenter, and the coordinate is determined according to the direction of the three-component sensor.

waveforms of hypocenters that have a certain distance from the sensor. We manually identify the arrival time amplitudes and the polarity of the *P*- and *S*-waves of 14 far-distance AE events. Fig. 13 shows the locations of the AE events compared with the visible position of fractures on the testing sample, which indicates that the locations based on the three-component AE sensor are within a reasonable range. However, the accuracy of the localization results still requires further investigation.

To effectively distinguish *P*- and *S*-waves, a sufficient propagation distance is required to create a discernible time difference between them. If this distance is too short, and and the time difference is less than the AE source's duration, *P*- and *S*-waves will overlap and become indistinguishable. Therefore, the time difference must exceed the AE source duration for effective differentiation. Current three-component sensors, with a lowest resonant frequency of 0.5 MHz, capture AE signals with a maximum duration of 2 μs. Considering the velocity difference of 1391 m/s between *P*- and *S*-waves, at least 2.78 mm of separation is necessary. However, these sensors often detect longer-period, lower-frequency signals around 0.1 MHz, indicating extended AE source durations. Under these conditions, a minimum separation distance of 13.91 mm from the AE source to the sensor is required to differentiate *P*- and *S*-waves. This limitation significantly constrains effective localization in smaller samples. Additionally, while three-component sensors provide comprehensive waveform data, the influence of anisotropy on these waveforms must also be considered. Extensive seismological research has been conducted on anisotropy's effects on waveforms, providing valuable insights for the application of three-component AE sensors.[35–39] Investigating the impact of anisotropy on AE signals is a significant focus for our future research.

5. Conclusions

In this paper, we fabricate a three-component AE sensor to monitor the rock fracturing processes. The results are compared with the commonly used single-component AE sensors. This is the first time a three-component AE sensor has been utilized and tested in laboratory experiments. The reliability of the three-component sensor is assessed by using an ultrasonic source and ball drop testing. The application of the three-component sensor in the uniaxial compression testing of a shale specimen indicates that the three-component waveforms can promote the analysis of complicated wave fields and provide a new and powerful approach to studying the multiple mechanism hypocenter of fractures in the rock failure process. The rectilinear, dip angle, and azimuth angle of the three-component waveforms can help distinguish the different waveform phases, although at present it is still difficult to quantify the changes in the polarization parameters involving different phases. In the uniaxial compression test, the three-component waveforms in the elastic and plastic stage contain information on multiple mechanisms of fractures, which cannot be collected in single-component AE sensors. The three-component sensor supports the calculation of AE location, which provides a new monitoring strategy for more information about the location and focal mechanism of AE events in rocks, especially in small-size samples.

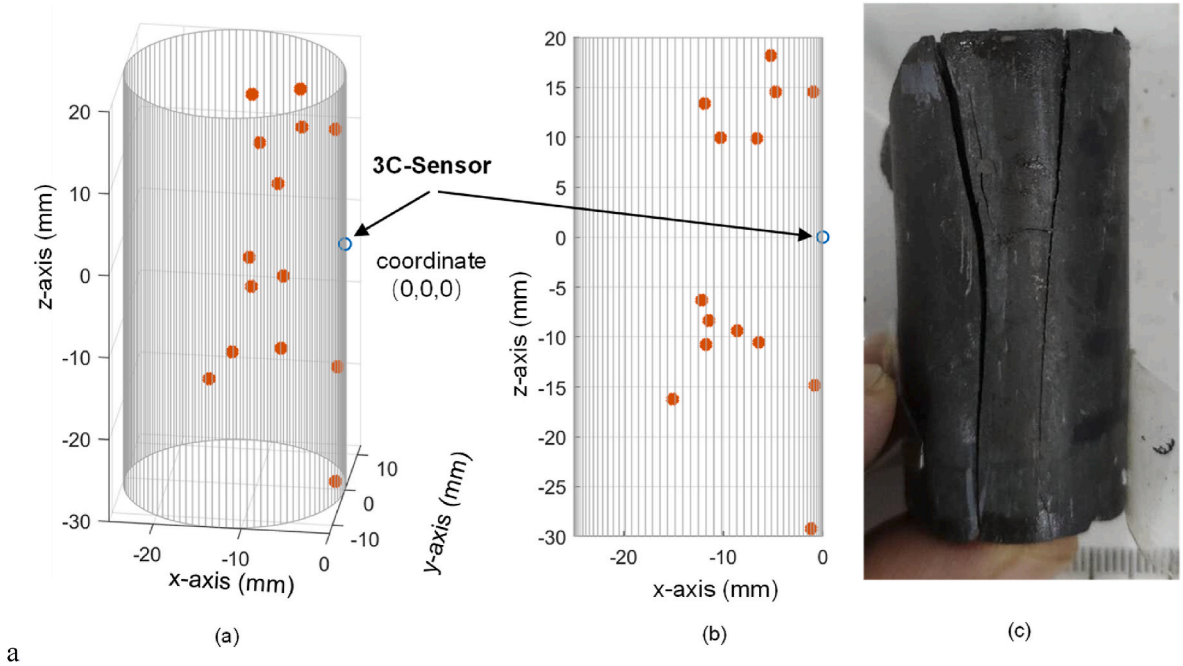

Fig. 13. AE location results based on the data obtained from the three-component sensor.

CRediT authorship contribution statement

Shan Wu: Writing – original draft, Software, Investigation. **Ke Gao:** Writing – review & editing, Validation, Supervision. **Yunyi Qian:** Methodology, Investigation. **Hongkui Ge:** Supervision, Methodology, Conceptualization. **Xiaoqiong Wang:** Writing – review & editing, Resources. **Tiantai Li:** Supervision, Resources.

Declaration of competing interest

The authors declare that they have no known competing financial interests or personal relationships that could have appeared to influence the work reported in this paper.

Data availability

Data will be made available on request.

Acknowledgments

The authors express thanks for financial support from the subprojects of the Natural Science Foundation of China (No. 42302326), the Collaborative Research and Innovation in the Yangtze River Delta (China) Science and Technology Community (No.2022CSJGG1200), and the Fundamental Research Funds for the Central Universities (JZ2023HGQA0145 and JZ2023HGTA0178).

References

1. Lockner D. The role of acoustic emission in the study of rock fracture. In: *International Journal of Rock Mechanics and Mining Sciences & Geomechanics Abstracts*. Elsevier; 1993:883–899, 30.
2. Wang X, Ge H, Song L, He T, Xin W. Experimental study of two types of rock sample acoustic emission events and Kaiser effect point recognition approach. *Chin J Rock Mech Eng*. 2011;30(3):580–588.
3. Lei X, Ma S. Laboratory acoustic emission study for earthquake generation process. *Earthq Sci*. 2014;27(6):627–646.
4. Ma K, Feng B, Zhuang D, Guo X, Gao Q. Distance effects of the fault on the surrounding rock mass stability of the main powerhouse at the Huanggou pumped-storage power station. *Tunn Undergr Space Technol*. 2020;106, 103568.
5. Carpinteri A, Lacidogna G. *Acoustic Emission and Critical Phenomena: From Structural Mechanics to Geophysics*. CRC Press; 2008.
6. Grosse CU, Ohtsu M. *Acoustic Emission Testing*. Springer Science & Business Media; 2008.
7. Aki K, Richards PG. *Quantitive Seismology*. second ed. Sausalito: University Science Books; 2002.
8. Lei XL, Kusunose K, Nishizawa O, Cho A, Satoh T. On the spatio-temporal distribution of acoustic emissions in two granitic rocks under triaxial compression: the role of pre-existing cracks. *Geophys Res Lett*. 2000;27(13):1997–2000.
9. Ohtsu M. Elastic wave methods for NDE in concrete based on generalized theory of acoustic emission. *Construct Build Mater*. 2016;122:845–854.
10. Goodfellow SD, Flynn JW, Young RP, Consultants AS, Kingdom U. Acquisition of complete acoustic emission amplitude records during rock fracture experiments. *J Acoust Emiss*. 2014;32:1–11.
11. Ono K. Calibration methods of acoustic emission sensors. *Materials*. 2016;9(7), 508-508.
12. Ma K, Sun X, Tang C, Yuan F, Wang S, Chen T. Floor water inrush analysis based on mechanical failure characters and microseismic monitoring. *Tunn Undergr Space Technol*. 2021;108, 103698.
13. Aggelis DG, Shiotani T, Terazawa M. Assessment of construction joint effect in full-scale concrete beams by acoustic emission activity. *J Eng Mech*. 2010;136(7):906–912.
14. Yoshimitsu N, Furumura T, Maeda T. Geometric effect on a laboratory-scale wavefield inferred from a three-dimensional numerical simulation. *J Appl Geophys*. 2016;132:184–192.
15. Zou Y, Li N, Ma X, Zhang S, Li S. Experimental study on the growth behavior of supercritical CO_2 induced fractures in a layered tight sandstone formation. *J Nat Gas Sci Eng*. 2018;49(September 2017):145–156.
16. Ohtsu M. Simplified moment tensor analysis and unified decomposition of acoustic emission source: application to in situ hydrofracturing test. *J Geophys Res Solid Earth*. 1991;96(B4):6211–6221.
17. Hardebeck JL, Shearer PM. Using S/P amplitude ratios to constrain the focal mechanisms of small earthquakes. *Bull Seismol Soc Am*. 2003;93(6):2434–2444.
18. Walter W, Ford S, Xu H, et al. Insights from the source physics experiments on P/S amplitude ratio methods of identifying explosions in a background of earthquakes. In: *AGU Fall Meeting Abstracts*. 2012:S23A–S2538, 2012.
19. Zhou W, Wang L, Guan L, Guo Q, Cui S, Yu B. Microseismic event location using an inverse method of joint P–S phase arrival difference and P-wave arrival difference in a borehole system. *J Geophys Eng*. 2015;12(2):14733–14739.
20. Wu S, Li T, Ge H, Wang X, Li N, Sun Y. New acoustic emission parameters for hydraulic fracture network description based on shear-tensile crack model. In: *53rd US Rock Mechanics/Geomechanics Symposium*. American Rock Mechanics Association; 2019.
21. McLaskey GC, Lockner DA, Kilgore BD, Beeler NM. A robust calibration technique for acoustic emission systems based on momentum transfer from a ball drop. *Bull Seismol Soc Am*. 2015;105(1):257–271.
22. Chen Q, Yin J, Yang Y. Time-frequency characteristic analysis of six-degree-freedom ground motion records. *Chin Q Mech*. 2014;35(3):499–506.
23. McLaskey GC, Glaser SD. Acoustic emission sensor calibration for absolute source measurements. *J Nondestr Eval*. 2012;31(2):157–168.
24. Flinn E. Signal analysis using rectilinearity and direction of particle motion. *Proc IEEE*. 1965;53(12):1874–1876.
25. Jurkevics A. Polarization analysis of three-component array data. *Bull Seismol Soc Am*. 1988;78(5):1725–1743.
26. Thorne L, Wallace TC. *Modern Global Seismology*. Academic Press; 1995.
27. Montalbetti JF, Kanasewich ER. Enhancement of teleseismic body phases with a polarization filter. *Geophys J Int*. 2010;21(2):119–129.
28. Benhama A, Cliet C, Dubesset M. Study and application of spatial directional filtering in three component recordings. *Geophys Prospect*. 1988;36:591–613.
29. Kanasewich ER. *Time Sequence Analysis in Geophysics*. University of Alberta; 1981.
30. Yurikov A, Nourifard N, Pervukhina M, Lebedev M. Laboratory ultrasonic measurements: shear transducers for compressional waves. *Lead Edge*. 2019;38:392–399.
31. Gu C, Mok U, Marzouk YM, et al. Bayesian waveform-based calibration of high-pressure acoustic emission systems with ball drop measurements. *Geophys J Int*. 2020;221(1):20–36.
32. Wu S, Ge H, Wang X, Meng F. Shale failure processes and spatial distribution of fractures obtained by AE monitoring. *J Nat Gas Sci Eng*. 2017;41:82–92.
33. McLaskey G, Glaser S. Nanoseismic measurement of the localized initiation of sliding friction. *Meso-scale Shear Physics in Earthquake and Landslide Mechanics*. 2009:31–42.
34. McLaskey GC, Glaser SD, Grosse CU. Integrating broadband high-fidelity acoustic emission sensors and array processing to study drying shrinkage cracking in concrete. In: *Sensors and Smart Structures Technologies for Civil, Mechanical, and Aerospace Systems 2007*. SPIE; 2007:150–161, 6529.
35. Vavryčuk V. Moment tensor decompositions revisited. *J Seismol*. 2015;19(1):231–252.
36. Leaney S, Yu X, Chapman C, et al. Anisotropic moment tensor inversion and visualization applied to a dual well monitoring survey. *Canadian Society of Exploration Geophysicists Recorder*. 2014;39:48–54.
37. Warner M, Ratcliffe A, Nangoo T, et al. Anisotropic 3D full-waveform inversion. 2013;78(2).
38. Chapman C, Leaney W. A new moment-tensor decomposition for seismic events in anisotropic media. *Geophys J Int*. 2012;188(1):343–370.
39. Anderson DL. Elastic wave propagation in layered anisotropic media. *J Geophys Res*. 1961;66(9):2953–2963.
40. Yang H, Duan HF, Zhu J. Experimental study on the role of clay mineral and water saturation in ultrasonic P-wave behaviours across individual filled rock joints. *Int J Rock Mech Min Sci*. 2023;168, 105393.